Journal of Imaging Science and Technology® 66(3): 030510-1–030510-20, 2022.

Modelling of A New X-Ray Backscatter Imaging System: Simulation Investigation

Selvagumar Senthurran, W. T. Yuen Peter, and Umair Soori
Cranfield University, Defence Academy of UK, Centre for Electronic Warfare, Shrivenham Swindon SN6 8LA, UK
E-mail: s.selvagumar@cranfield.ac.uk

Jonathan Piper
Defence Science and Technology Laboratory (DSTL), Space and Sensing Systems Group, Porton Down, Salisbury, Wiltshire SP4 0JQ, UK

James David, Daniel Andre, and Mark Richardson
Cranfield University, Defence Academy of UK, Centre for Electronic Warfare, Shrivenham Swindon SN6 8LA, UK

Abstract. *X-ray backscatter imaging is a powerful technique for medical, aerospace, and security applications. Conventionally, a pinhole is commonly used for focusing X-ray, but there is always a desire to enhance the signal-to-noise-ratio (SNR) and optical throughput compared to a single pinhole. The main aim of this paper is to present a new X-ray backscatter imaging system which was inspired by a Twisted Slit collimator system called the Vortex Collimator and compare the optical throughput and the imaging performance with that of the Twisted Slit' collimator [G. Jaenisch et al., "Scatter imaging – simulation of aperture focusing by deconvolution," (IEEE, Piscataway, NJ, 2017), p.301-306; G. Jaenisch, S. Kolkoori & C. Bellon, "Quantitative simulation of back scatter X-ray imaging and comparison to experiments," 1–11 (2016)] and the Pinhole imaging systems for axial point sources, where the pinhole system was used purely for comparison purposes. All the comparisons were performed through Ray tracing (TracePro) simulation software. This work shows that the Vortex design yields ∼4% higher SNR/optical throughput than that of the Twisted Slit collimator, and ∼42.5% higher transmittance. Furthermore, the opening of the Vortex Collimator was increased and reduced to observe the performance, resulting in about ∼1% transmittance increment when the opening was increased. Also, thicknesses of the Vortex Collimator and Twisted Slit collimator were increased and reduced and found that reducing the thickness appears to increase the system's throughput marginally.* © *2022 Society for Imaging Science and Technology.*
[DOI: 10.2352/J.ImagingSci.Technol.2022.66.3.030510]

1. INTRODUCTION

1.1 *Backscatter X-ray Imaging (BAXI)*

X-ray backscatter imaging (XBI) technology has attracted a lot of attention during the turn of the century and it has been applied for vehicle surveillance, IED detections and for detection of buried objects such as land mines. Unlike conventional transmission X-ray, which is more sensitive for detecting high atomic number material [1–3], BAXI relies on the Compton scattering of the X-ray with the core electrons [1, 2, 4, 5], and is more sensitive to low atomic number materials like explosives [2, 6]. Furthermore, BAXI is more attractive in operations as both the X-ray source and detector are mounted in the same housing; thereby, it can scan large objects [7]. When a photon collides and interacts with motionless electron [8], it will transfer some of its energy to that electron, and this phenomenon can be described as the Compton effect [9, 10]. The kinetic energy gained by the electron will force it to move off at some angle, and the scattered photon now has a smaller quantity of energy than before [11]. This suggests that the frequency of the scattered photon will drop while the wavelength increases [2, 12].

The backscatter technique is not to be confused with a traditional X-ray machine, which relies on the transmission of X-rays through the object [13, 14]. The backscatter pattern is dependent on the material property. It is suitable for imaging organic material, which means that objects with a low-atomic number (Z-number) such as Aluminum, Perspex, composites, and water exhibit predominant scattered radiation patterns compared to heavy metals such as heavy metals Fe, Cu, and Pb [15, 16]. Conventionally, a pinhole is used to focus X-rays, but unfortunately, the energy capacity is limited to only 10 keV. Focusing any radiation over 10 keV is possible in a limited way, such as (very narrow field of views and narrow-passbands) through a Laue diffraction lens [17–19]. A Laue lens concentrates using Bragg diffraction in the volume of many crystals arranged in concentric rings and accurately orientated to diffract radiation from infinity towards a common focus [20].

The pinhole imaging system produces the one-to-one ratio relationship between the object and the image because of its small size and dim and inverted image [8, 21]. The advantages of using the single pinhole system are that it is cheap and straightforward, can be used for any wavelength, and objects at any distance produce clear images (great "depth of field") [22]. The major disadvantage is low throughput, and hence low signal to noise ratio in the resulting images.

To overcome these problems, scientists were using other alternative approaches such as Coded aperture imaging,

Received July 29, 2021; accepted for publication Feb. 28, 2022; published online Apr. 4, 2022. Associate Editor: Xinghua Li.
1062-3701/2022/66(3)/030510/20/$25.00

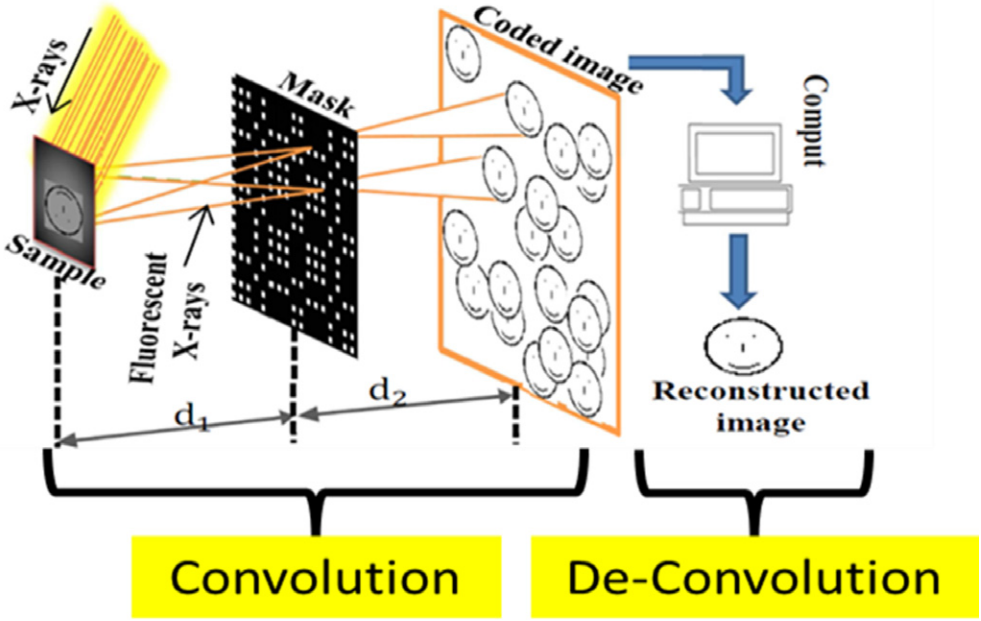

Figure 1. Coded aperture Convolution and De-convolution process.

which has been around for nearly three decades. The concept of using coded aperture for X-ray imaging was first introduced by Dicke, who replaced the single pinhole with many random openings [23, 24]. This imaging technique is also known as multiplexing imaging, a two-step process that is encoding and decoding [21] as shown in Figure 1.

$$\text{Encoding (Convoluted): } D = S * A + B, \quad (1)$$

$$\text{Decoding (De-Convoluted): } D * G = S^{\wedge} = S + B * G, \quad (2)$$

where * is the correlation operator, S represents the source, D is the observed image, A indicates the coded aperture (CA) structure, B represents all background contributions not modulated by the CA, $S^{\wedge}$ is the reconstructed image, $A * G =$ point spread function $= \delta$ and $B * G =$ residue function ordinarily small and can be neglected [21].

The illumination source is in all directions not parallel to the optical axis of the mask, thereby merging shadows from adjacent pinholes, causing a change of intensity below the pinhole.

Using such an imaging system is time-consuming and not ideal for mobile imaging as the detector sizes depend on the mask sizes. Most importantly, during nearfield imaging conditions, the nearfield image artefacts will play a significant part in the signal to noise ratio. An alternative approach of increasing the thickness of the single pinhole aperture has been considered, but unfortunately, it acts more like a collimator than a single pinhole imaging system [7, 25].

However, the new imaging system proposed by the German researchers in 2005 [26, 27], known as the Twisted Slit collimator concept, seems to fulfil all necessary requirements [26].

1.2 *Twisted Slit Collimator*

The Twisted Slit collimator can be described as a diaphragm with a virtually continuous series of holes with large angular aperture or in other words, the inside of the slit is lined with ruled surfaces; consequently, the linear passage of the backscatter radiation through the slit is possible only through a hole-shaped gap (Figure 2 shows the schematic of the Twisted Slit design) [16]. The gap is formed by the twisted surfaces of the upper and lower part of the collimator. The intersection of the front and back of the slit forms the beam passage, and tilting the aperture towards or away from the source, the beam passage is shifted to the right or left [28].

Early designs of the Twisted Slit camera were built of several lead bricks, weighing about 300 kg, and incorporated a phosphor imaging plate as the detector, which required an exposure time of approximately 30 min [27]. Further development yielded a simplified system using Tungsten which reduced the mass to 30 kg and a digital matrix detector with an exposure time of 40 s [2, 15]. Even though this design solves the problem of high energy radiation, the imaging time increases and the size and weight of the system limits its utility.

A current design with an exposure time of less than 60 s with improved image resolution can be used as a mobile device. For a perfect image, the slit width of the collimator can be varied from 0.1 mm to 2 mm with an angle of up to about 45° between an incident and scattered radiation directions for imaging [28] and is capable of withstanding X-ray energy from 50 keV to 600 keV [29]. Currently, this device is used for non-destructive field testing, for example, Impact damage on the CFRP (Carbon-fiber – reinforced polymer) skins [29], water inclusions between CFRP skin, core materials detection and structural Integrity can be imaged [29].

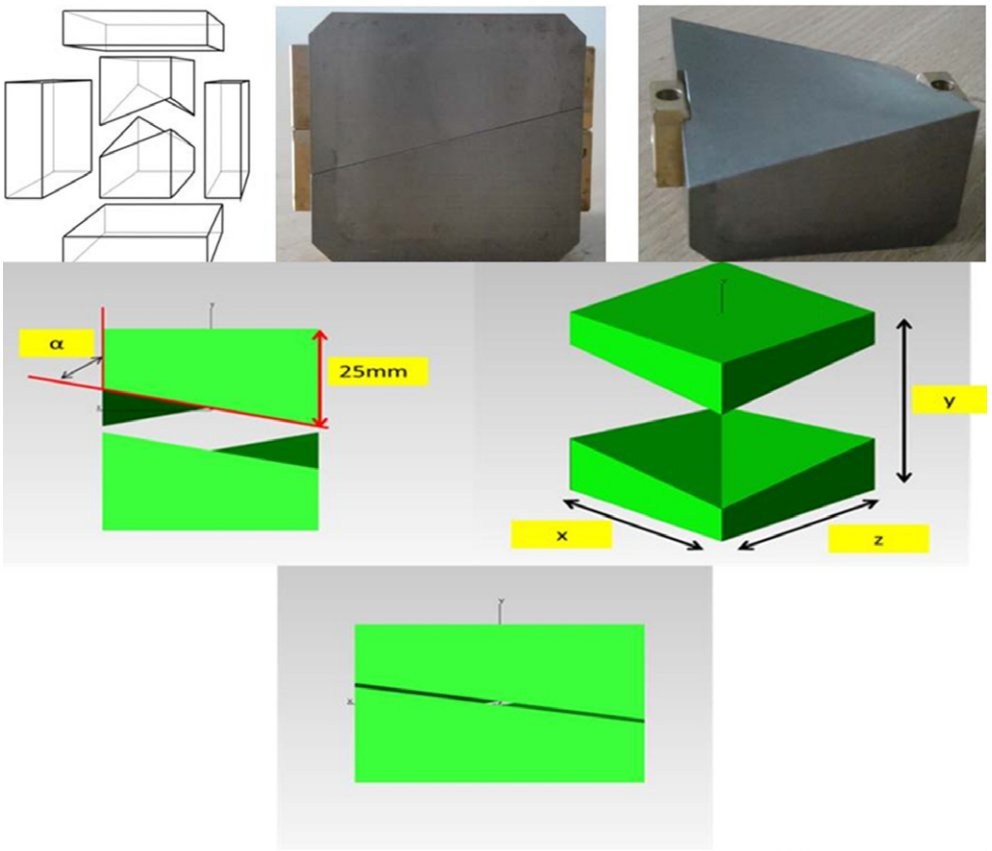

Figure 2. Twisted Slit collimator: top image is a basic layout of Twisted Slit collimator [3, 28]. The middle and bottom are the CAD model created for simulation.

However, the main disadvantage of using this design is the Field of View (FoV) restriction. It is possible to overcome this problem by increasing the slit opening size but at the cost of an increase in the background noise and blurry final results. Other notable disadvantages are distortion artefacts, the reduced beam opening and collimated X-ray source resulting in poor signal-to-noise ratio (SNR) as well as long measurement time. To be more cost-effective and fabrication friendly, with all these in mind, we came up with a new design and labeled it the Vortex Collimator.

1.3 *Signal to Noise Ratio (SNR) and Transmission Factor Calculation*

Regardless of how an image looks visually, it is essential to measure the quality of the image by a metric. It not only gives a scientific understanding but is also easy to compare and validate images. Therefore, in this case, we used the Signal Noise ratio (SNR), a standard measure used throughout the research field and on top of that, we also used the Transmission factor as a secondary measure to quantify the quality of the resulting images. Several SNR methods are available, and here the SNR is calculated by summing the signals and dividing by the sum of false positives [30, 31].

$$\mathrm{SNR} = 10 * \log 10 \times (\mathrm{Image}_{\mathrm{MEAN}}/\mathrm{Image}_{\mathrm{STANDARD\ DEVIATION}}) \tag{3}$$

$$\mathrm{SNR} = 10 * \log 10 \times \left(\left(\sum S\hat{}2\right) \Big/ \left(\sum N\hat{}2\right)\right) \tag{4}$$

$$\mathrm{SNR} = 10 * \log 10 \times \left(\sum_{0}^{n_x-1}\sum_{0}^{n_y-1}[r(x,y)]^2 \Big/ \sum_{0}^{n_x-1}\sum_{0}^{n_y-1}[r(x,y)-t(x,y)]^2\right) \tag{5}$$

$$\mathrm{RMSE} = \sqrt{\frac{1}{n_x n_y}\sum_{0}^{n_x-1}\sum_{0}^{n_y-1}[r(x,y)-t(x,y)]^2}, \tag{6}$$

where S is the signal and the N is the background noise (false positive), reference image $r(x, y)$ with a test $t(x, y)$ [31]. The two images must be of the same size $[nx, ny]$, and the Root Mean Square Error (RMSE) (also called the root mean square deviation, RMSD), a frequently used measure of the difference between values predicted by a model and the values observed from the environment that is being modelled. These formulas were verified using several other reference sources such as Gonzalez and Woods, "Digital

Image Processing", and Matlab image processing toolbox [9, 30]. SNR in these references is explained as a measure independent of the type of noise being analyzed, but the significance and usability of the parameter depend on the type of noise. SNR is useful in random and uniformly distributed noise (e.g. Gaussian), but images with other nonlinear noises (e.g. degradation between a threshold or degradation in a specific area and not the whole image) could give unreliable results [7, 32].

Secondly, measuring the image quality by using transmission factor (%), where the transmission factor of a medium T can be defined as the ratio of the radiation flux Φ passing through the medium to the flux Φ_0 incident upon the surface of the medium [33, 34]:

$$T = \frac{\Phi}{\Phi_0}. \tag{7}$$

The transmission factor concept is frequently used in relation to illumination flux [35]. This factor depends on several criteria such as the body's dimensions, shape, surface condition, angle of incidence, spectral composition, and polarization of the incident radiation [36, 37]. A distinction is made between transmission factors for direct transmission, in which the medium does not scatter the radiation passing through it; for diffuse transmission, in which the medium diffuses all radiation penetrating it; and for mixed transmission, in which there is partial diffusion [38].

2. DEVELOPMENT OF A NEW X-RAY IMAGING TECHNIQUE

2.1 *Vortex Collimator Design Methodology*

Inspired by the Twisted Slit collimator, the Vortex Collimator is a design introduced as an auxiliary imaging technique for a single pinhole imaging system in high-energy X-ray imaging and similar environments. The Vortex Collimator was named by virtue of its internal surface features, such as swiped and twisted, which contains similarities of a Vortex flow. Like the Twisted Slit collimator, this system was designed to attenuate background rays, and provide a 2D image of the subject.

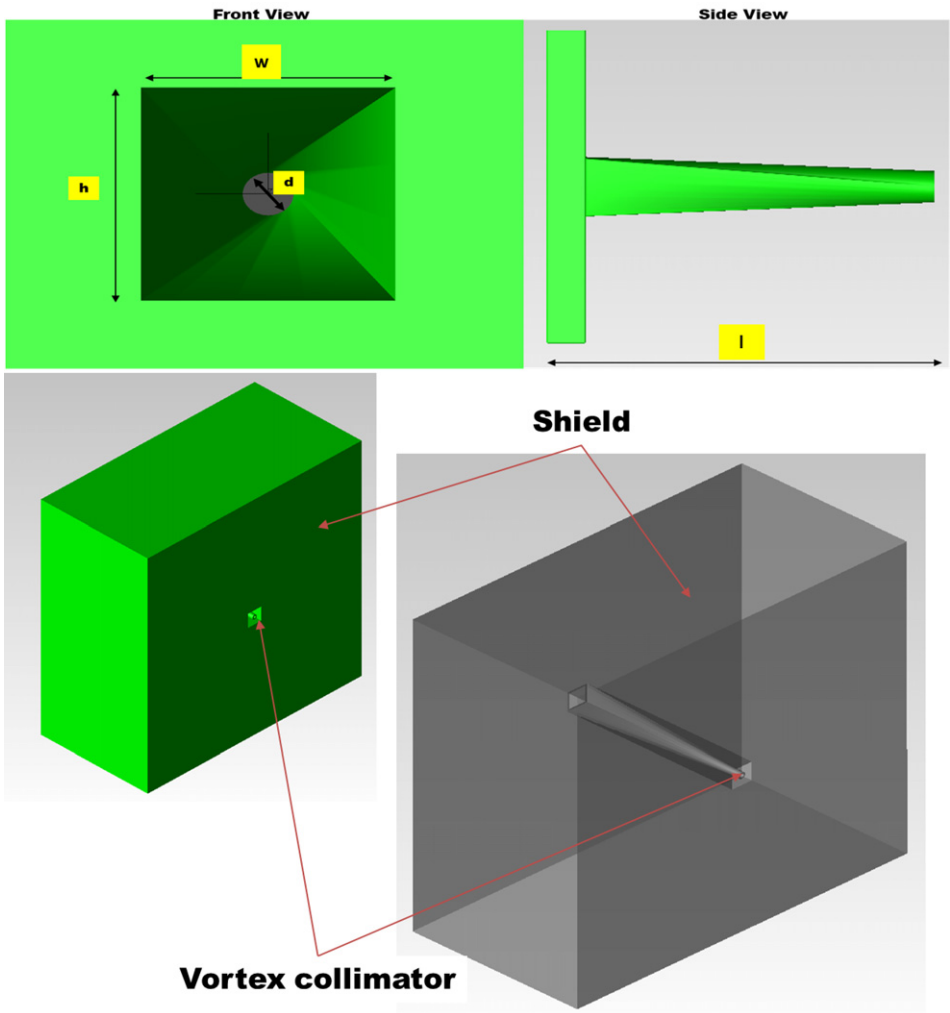

Figure 3. Vortex Collimator design representation.

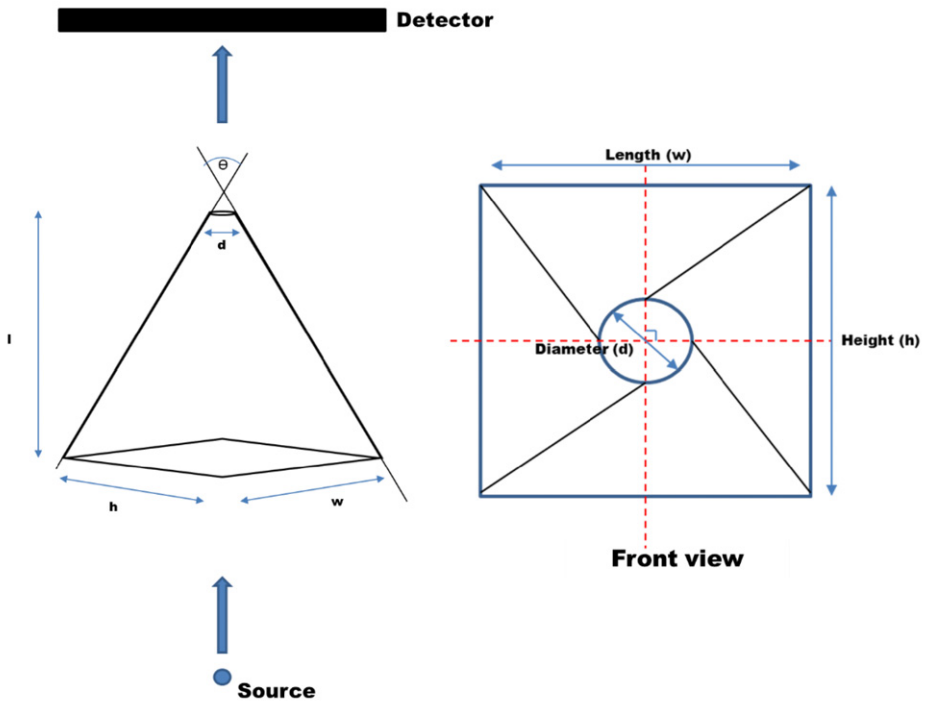

Figure 4. 2D internal view and dimensions of Vortex Collimator.

In general, parallel hole collimators are used to collimate X-rays [39, 40]; although they improve resolution, they also reduce intensity by blocking incoming radiation, which is undesirable for remote sensing instruments requiring high sensitivity, encouraging us to come up with this particular design. This was first designed using the Creo (Pro-Engineer) 3-dimensional (3D) modelling software as shown in Figure 3 and then TracePro raytracing software for further simulation.

As mentioned above, the Vortex Collimator represents a Vortex flow, and the idea was inspired by a simple 3D-iris design. The Vortex Collimator will have a wider opening, in this case, a square opening on one side and the other side will be a circular outlet/exit to the requirements (either 0.5 mm/1 mm/2 mm . . .), which in this case is 1 mm, in order for a like-for-like comparison with Twisted Slit collimator and Single pinhole. However, unlike the Twisted Slit collimator, the depth/length of this design l is independent of object design parameters such as height, width, and wall thickness. As shown in Fig. 3 and Figure 4, the current design has a square opening, which is $h = 5$ mm and $w = 5$ mm. The design has an opening area of 25 mm^2, exit area of 0.785 mm^2 with an end diameter of 1 mm, the design width (design depth) $l = 50$ mm and an angle of 10° (can vary between 5° and 50°) between the incident and scattered radiation directions for imaging. However, this can be changed contingent on the imaging requirements.

Another essential measure to define the quality of a collimator is the spatial resolution, which is a significant system property and is defined as the full-width-at-half-maximum (FWHM) of the point spread function (PSF), which is determined by the intrinsic detector resolution and the geometrical resolution of the collimator. This spatial resolution measurement of the collimator $R_{\text{collimator}}$ can be defined as:

$$R_{\text{collimator}} = d_{l/2} + (d * s)/l_{\text{effective}}, \tag{8}$$

where the collimator length (or depth) l, hole diameter $d_{l/2}$ defines hole diameter as half the length of the collimator and distance from the radiation source to the collimator s. And the $l_{\text{effective}}$ can be defined as [41, 42]:

$$l_{\text{effective}} = l - 2/\mu, \tag{9}$$

where μ is the linear attenuation coefficient of the material from which the collimator is made [43–45]. Which in our case $l_{\text{effective}} = 40.52$ mm and $R_{\text{collimator}} = 21.74$ mm. And the geometric efficiency, which the fraction of emitted photons that pass through the circular aperture of the collimator, can be defined as [46]:

$$G_{\text{efficiency}} = \frac{d^3 \sin^3 \alpha}{16h^2}, \tag{10}$$

where d is the diameter of the pinhole, h is the perpendicular distance from the aperture to the source, and α is the incidence angle of the photon on the aperture plane at the center of the aperture [46–48].

3. RESULTS AND DISCUSSION

3.1 *Experimental Setup*

Once the design was finalized, it was modelled using the Creo (Pro-Engineer) 3D design and modelling software. It was uploaded into TracePro raytracing software for further

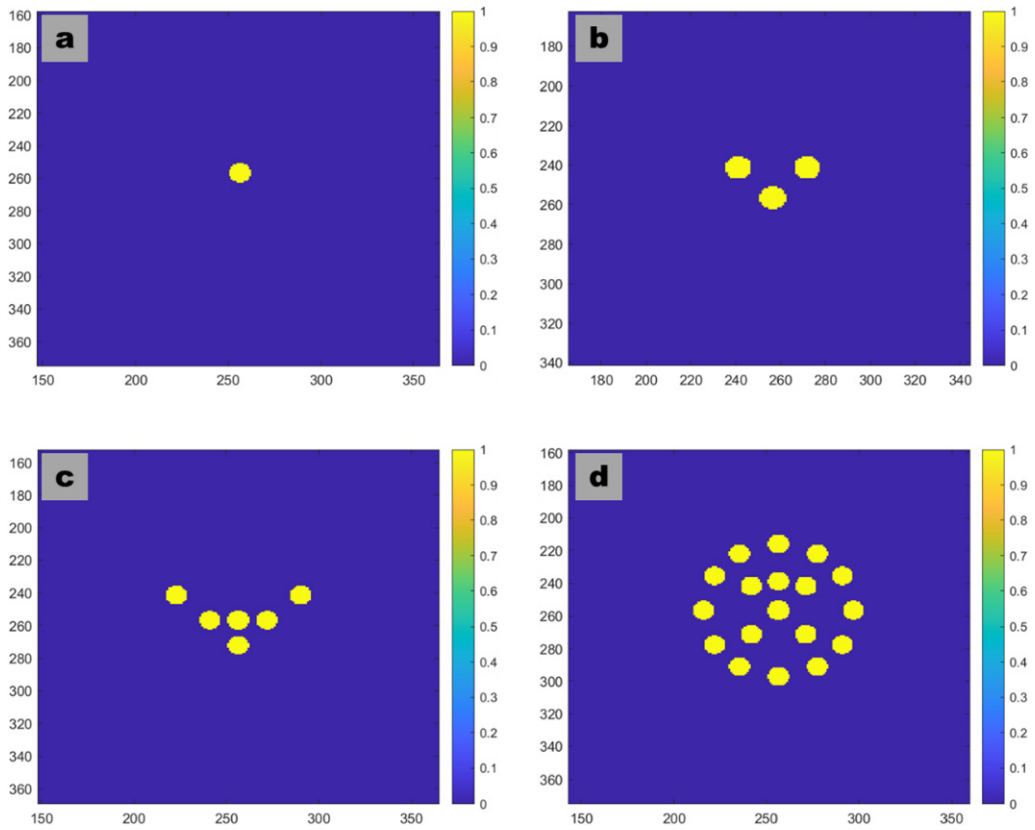

Figure 5. Source images used for the simulation (a) single point source (b) 3 Dot source (c) arrow source and (d) smiling face (the images have been zoomed-in for a clear view).

investigations and to compare with Single Pinhole, which is 1 mm in thickness with a 1 mm hole size and Twisted Slit Collimator with 50 mm × 50 mm × 50 mm cube, where Single Pinhole was used purely for reference/comparison purposes and assumed that it could absorb high energy radiation. Also, for a fair and like for like comparison, both Twisted Slit collimator and Vortex Collimator were designed to have the same thickness of 50 mm and an exit aperture area of 0.785 mm^2.

For this simulation, four illuminated sources with varying fields of view were used, respectively; Single point source (PHS), 3 Dot source (3Dot), Arrow source, and Smiling face source, as shown in Figure 5. To reduce the computational time, the diameter of these sources was kept between 1 mm and 9 mm, and are the ideal minimum to maximum sizes for the propagation of 750 kWatt to 13.5 MWatt (please refer to Table I), respectively, with a wavelength of 0.0021 nm. Once the sources were uploaded to the raytracing software along with the single pinhole imaging system and Twisted slit collimator imaging systems Figure 6, the simulations were conducted to identify the best imaging system (this setup is shown in Figure 7).

Fig. 7 is an illustration of how the experiment was set up. This image elaborates an example of Twisted Slit collimator in a simulation setup with a 400 mm distance from the imaging system (Twisted Slit collimator) and 400 mm from the imaging system to the detector. The detector has

Table I. Source modelling.

Sources	Flux (W)
Pinhole source	748501
2 Dot source	1497000
3 Dot source	2245500
Arrow source	4491010
Smiling face source	13473000

dimensions of 50 × 50 mm with 512 × 512 and a 0.096 mm pitch, was constructed as a perfect absorber of solid objects with a top-hat quantum efficiency of 100% across the spectral region of interest (ROI). For simulation, self-illumining sources were used, where the rays propagate from and travel through the mask and were then collected on the detector. After the convolution data were collected from TracePro, they were transferred to Matlab for further processing and calculation of the signal-to-noise ratio and the throughput of each result. The calculated results were then compared to determine the best system for focusing imaging technique.

In Figure 8 top image indicated as A. describes the ray diagram, and the bottom image indicated as B. shows the ray diagram of the Vortex Collimator. From these images, the most critical characteristic difference is the ray scattering. It is obvious that the ray through the Vortex Collimator tends

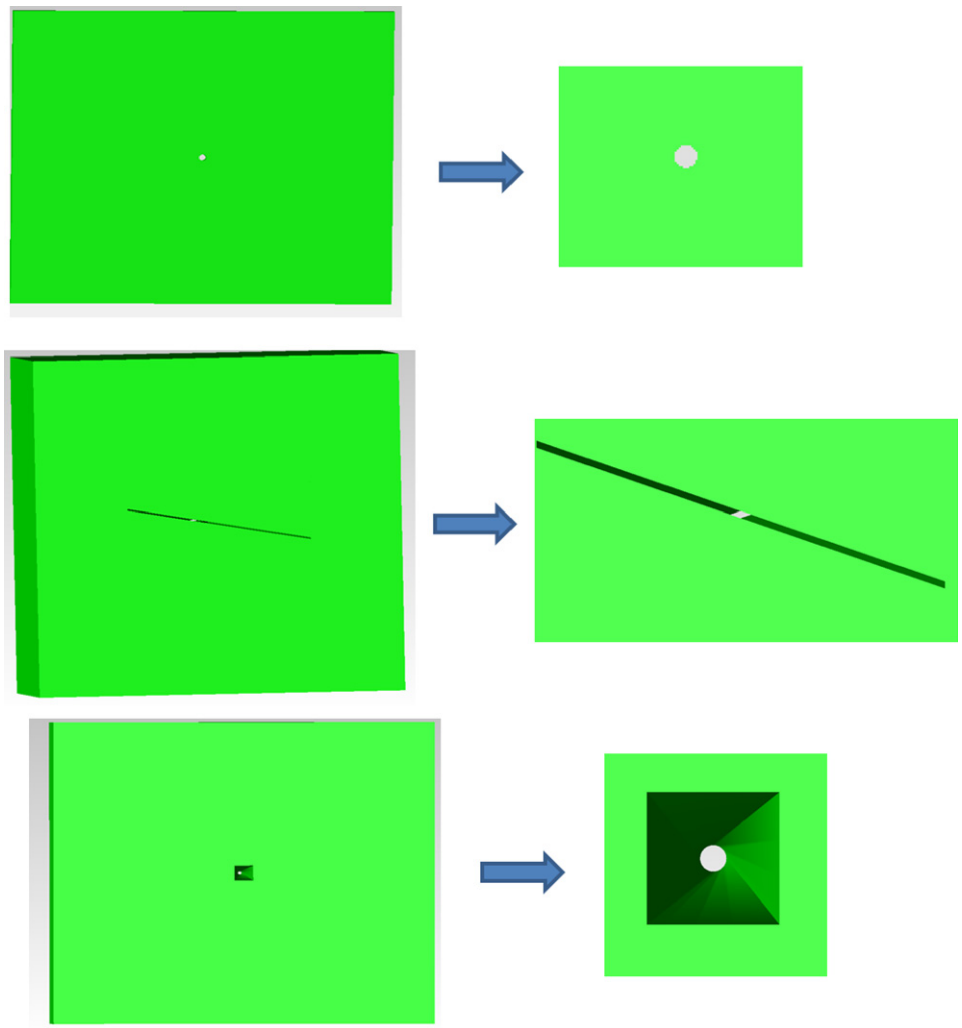

Figure 6. Imaging systems on the left and their front views on the right: (top) single pinhole mask (middle) Twisted slit collimator (bottom) Vortex Collimator (material properties are of Tungsten for all three).

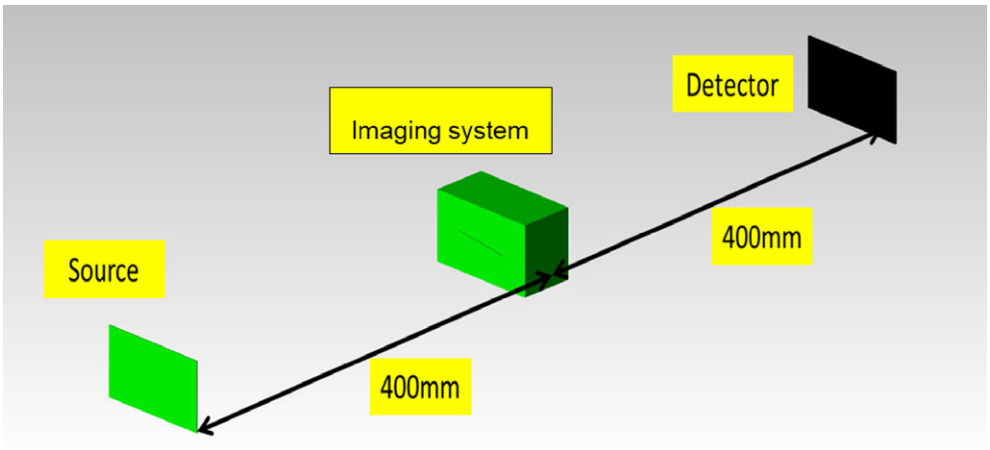

Figure 7. TracePro experimental simulation setup.

to scatter away from the sensor, and for the same size sensor, the ray through the Twisted Slit collimator seems to scatter onto the sensor and induces background noise. Even though the flux of the ray that reaches the sensor is low, it will still affect the quality of the image. This can be avoided by increasing the slit size, but that will compromise the image

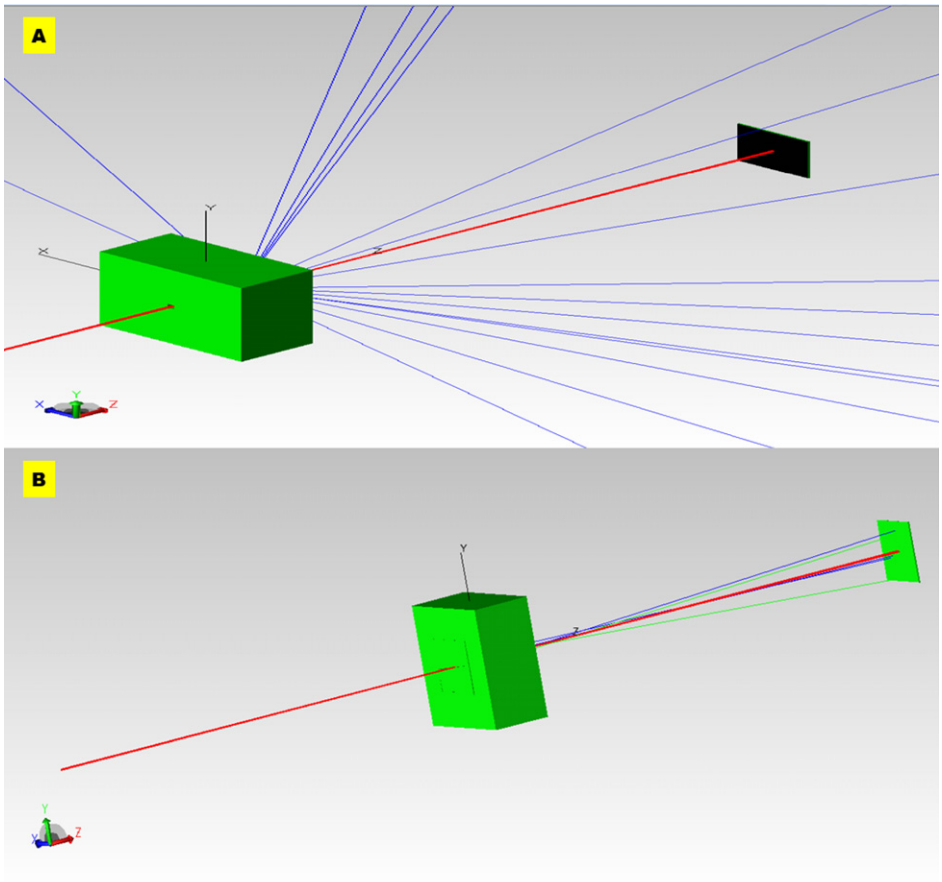

Figure 8. Top image A indicates the Vortex Collimator ray diagram, and bottom image B indicates the Twisted Slit ray diagram.

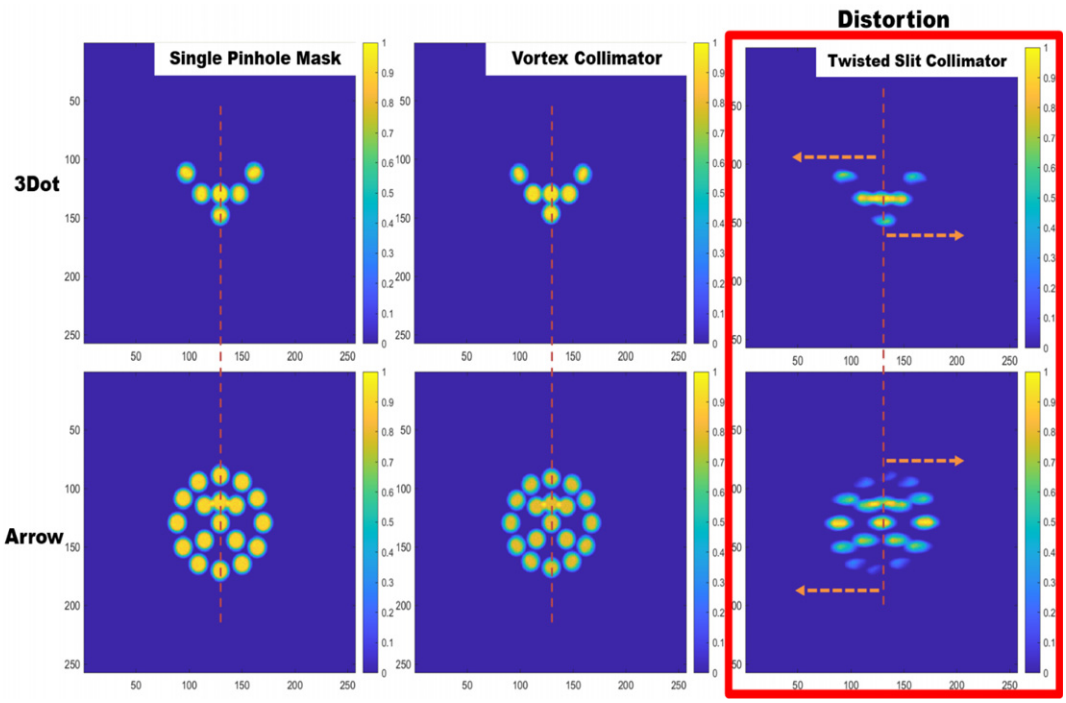

Figure 9. Raw simulation results of Single Pinhole, Vortex Collimator, and Twisted Slit collimator. Also, the example of Twisted Slit shift demonstration (0.0021 nm ~ 600 keV).

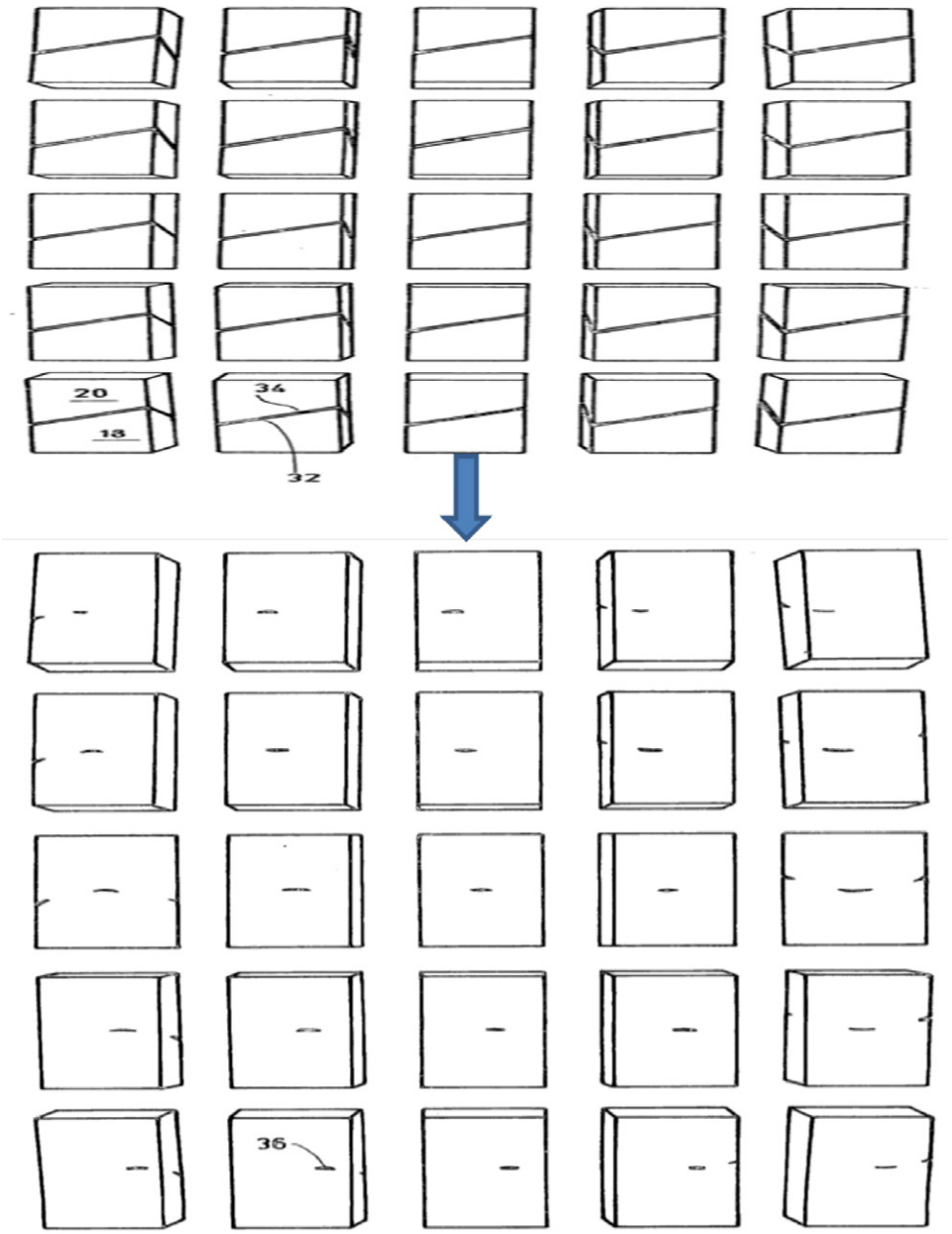

Figure 10. Perspective distortion of Twisted collimator from different field-of-view [26].

qualities such as the sharpness of the image and for much bigger sources (higher diameter sources), will induce more background noise.

The images in Figure 9 show the outcome of TracePro raw (without correcting distortion) simulation results for single pinhole, Twisted slit, and Vortex Collimator designs. The vertical dotted line indicates the vertical alignment of the results. The Vortex Collimator and Single Pinhole Mask results behave similarly without distortions for the current simulation boundary conditions. The Twisted Slit collimator, however, demonstrates geometric distortion [49]. Furthermore, these phenomena are indicated by arrows in Fig. 9 titled as Twisted Slit collimator, which describes the distortion's direction. This phenomenon is elaborated by Figure 10 and Figure 11, which shows that the opening of the Twisted Slit collimator moves depending on the direction of the incoming ray.

Fig. 11 is an attempt to demonstrate how the Twisted Slit collimator will view the source with different view angles, in other words, the field of view of the source. Due to several software restrictions, instead of changing the source field of view, we changed the angle of the imaging system by tilting, in this case, Twisted Slit collimator. Twisted Slit collimator distortion was demonstrated by tilting the structure by 0°, 3°, and 5°, respectively, as examples; and as shown, when the system is tilted, the opening of the

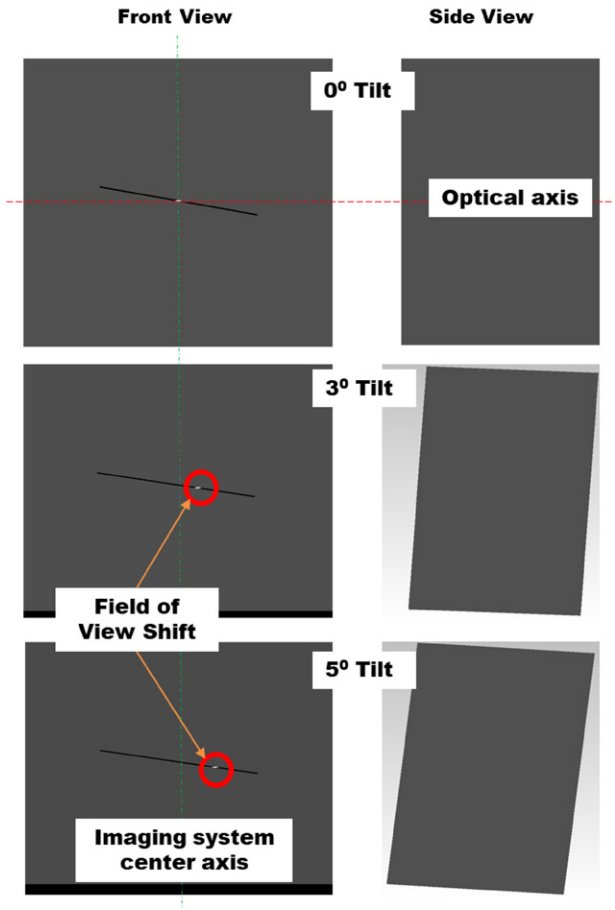

Figure 11. Twisted Slit field of view demonstration in Trace pro.

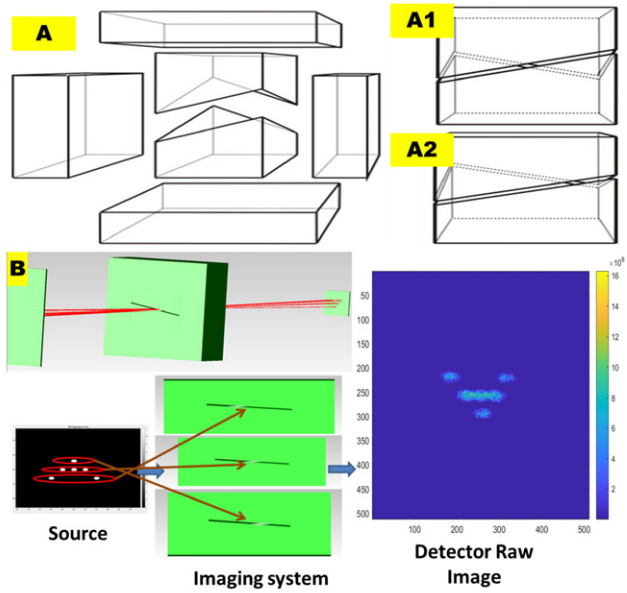

Figure 12. Twisted Slit collimator distortion (A) is a 3-Dimensional view of the Twisted Slit collimator A1 and A2: field of view demonstration [28, 29] (B) an example of perspective distortion of the Twisted collimator for Arrow Source with ray tracing and view angles.

imaging system shifts. Nevertheless, in reality, the process is reversed, where the Imaging system will remain static, and the field of view of the source will change, which will result in the same phenomena/distortion. This phenomenon is also demonstrated in Figure 12.

Perspective distortion is a warping or transformation of an object and its surrounding area that differs significantly from what the object would look like due to the relative scale of nearby and distant features, demonstrated by raytracing software in Fig. 12 and Figure 13. These images also show how the inside of the slit is lined with the ruled surfaces, and part A shows how the design looks like before they connect, part B shows how the gap is formed when the Twisted surfaces of the upper and lower part the collimator come together. Finally, part C shows how the beam passage shifts when the Twisted Slit imaging system is tilted. In this case, the aperture is tilted towards the source; therefore, the beam passage is shifted to the right.

Based on this scenario, it was easy to understand how distortion occurs in the resulting final image. For example, if we consider a source such as a Smiling face source with a diameter of 9 mm, as shown in Fig. 12, the center three points of the source are on the optical axis, and the other points are above and below the optical axis. As can be seen, the point of view or the view angle of the source and the corresponding Twisted Slit tilts is given by Fig. 12B (bottom left), and the result is shown on the right side of the detector image. Furthermore, as explained previously, in this case, the aperture remains the same, and the angle of view of the source changes; therefore, distortion occurs, which is also demonstrated by Fig. 12 and Fig. 13.

Fig. 13 shows the raw images collected on the sensor for the Twisted Slit collimator indicated as A (top part of Fig. 13) and for Vortex Collimator indicated as B (bottom of the image) and the corresponding 2D profiles beside each result. Moreover, as mentioned above, it is apparent how the distortion due to Twisted Slit collimator affects the final results. Once this problem was identified and analyzed, a MATLAB-based Affine Transformation algorithm was developed and was used to correct the distortion for a fair comparison with other mask results. Applying an affine transformation to a uniformly distorted image can correct a range of perspective distortions by transforming the measurements from the ideal coordinates to those used [50, 51]. This phenomenon is demonstrated in Figure 14 where the image on the left is distorted, and the one on the right is the transformed image.

Affine transformation is a linear mapping method that preserves points, straight lines, and planes [50, 52]. Sets of parallel lines remain parallel after an affine transformation. The affine transformation technique is typically used to correct for geometric distortions or deformations with non-ideal camera angles [49]. An affine transformation is an essential class of linear 2-D geometric transformations that maps variables (e.g. pixel intensity values located at position (x_1, y_1) in an input image) into new variables

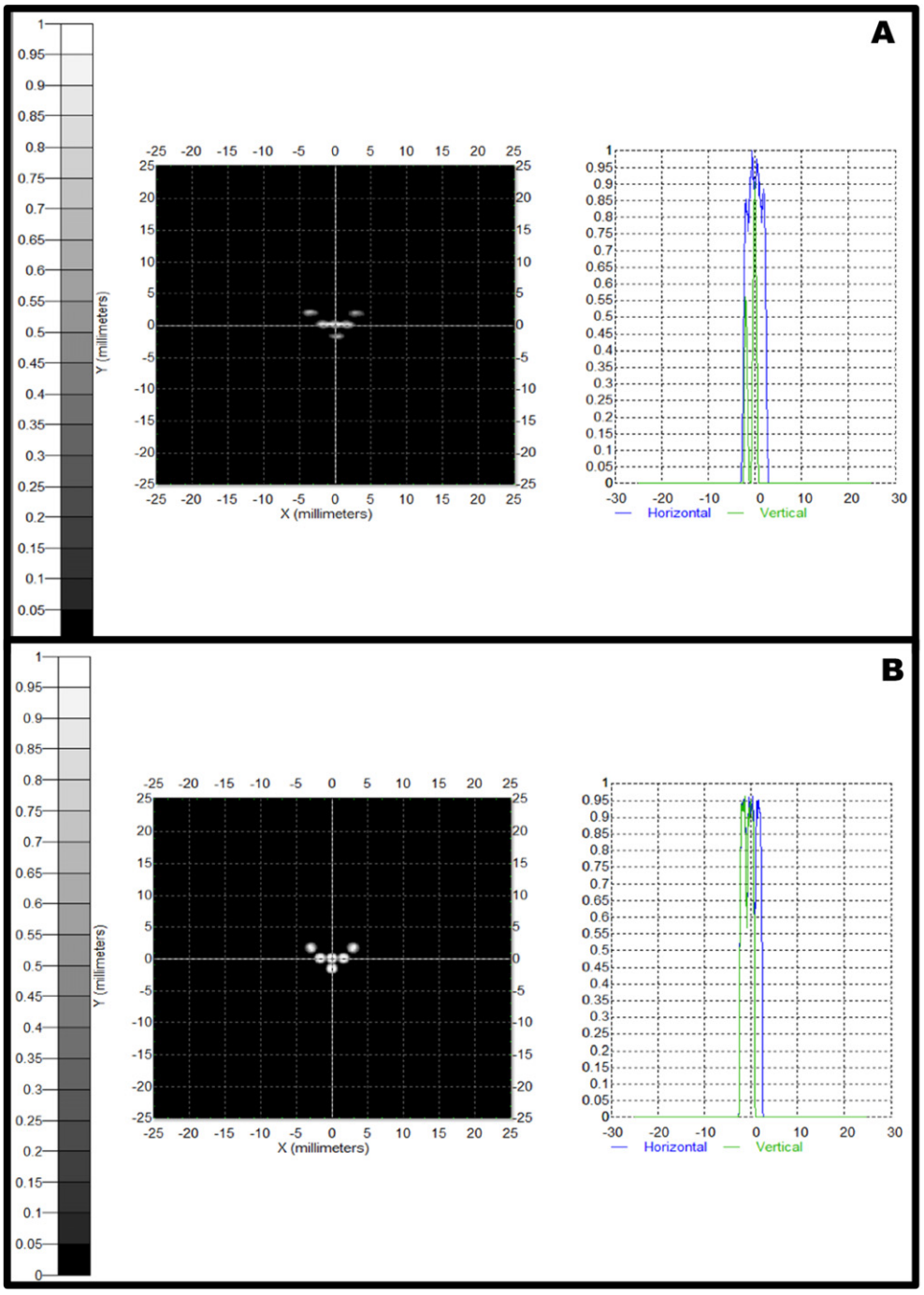

Figure 13. The simulation comparison of (A) Twisted Slit collimator sensor reading and the 2D profile and (B) Vortex Collimator sensor reading and the 2D profile.

(e.g. (x_2, y_2) in an output image) by applying a linear combination of translation, rotation, scaling and/or shearing (i.e. non-uniform scaling in some directions) operations [51, 53, 54].

The general affine transformation is commonly written in homogeneous coordinates as shown below [50]:

$$\begin{vmatrix} x_2 \\ y_2 \end{vmatrix} = AX \begin{vmatrix} x_1 \\ y_1 \end{vmatrix} + B. \tag{11}$$

By defining only the $\boldsymbol{B}$ matrix, this transformation can carry out pure translation [49]:

$$A = \begin{vmatrix} 1 & 0 \\ 0 & 1 \end{vmatrix}, \quad B = \begin{vmatrix} b_1 \\ b_2 \end{vmatrix}. \tag{12}$$

Pure rotation uses the $\boldsymbol{A}$ matrix and is defined as (for positive angle being clockwise rotation) [49]:

$$A = \begin{vmatrix} \cos(\theta) & -\sin(\theta) \\ \sin(\theta) & \cos(\theta) \end{vmatrix}, \quad B = \begin{vmatrix} 0 \\ 0 \end{vmatrix}. \tag{13}$$

Figure 14. Affine transformation demonstration.

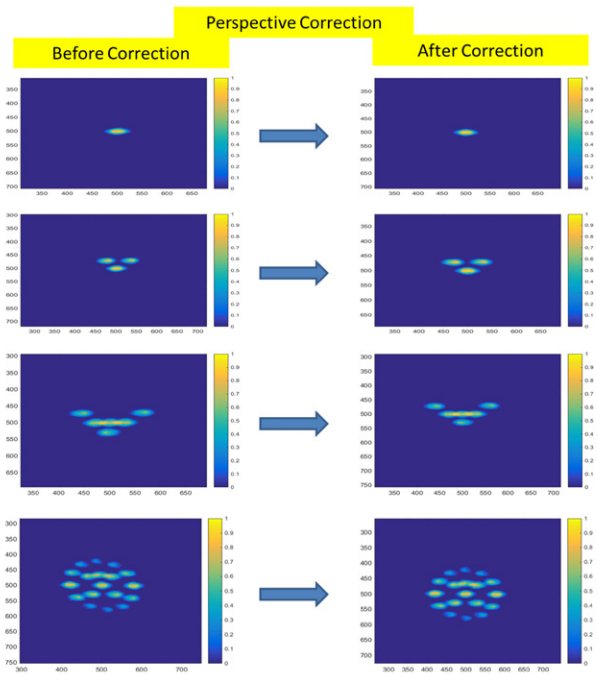

Figure 15. Before and after correction images of perspective distortion for Twisted Slit collimator.

As we are working in image coordinates, the y axis goes downwards. The rotation formula can be defined for when the y axis goes upwards. Similarly, pure scaling is [49]:

$$A = \begin{vmatrix} a_{11} & 0 \\ 0 & a_{22} \end{vmatrix}, \quad B = \begin{vmatrix} 0 \\ 0 \end{vmatrix}. \tag{14}$$

It is important to note that several different affine transformations are often combined to produce a resultant transformation [49, 52]. The order in which the transformations occur is significant since a translation followed by a rotation is not necessarily equivalent to the converse [55]. Since six constants define the general affine transformation, it is possible to define this transformation by specifying the new output image locations (x_2, y_2) of any three input image coordinate (x_1, y_1) pairs. (In practice, many more points are measured and the least-squares method is used to find the best fitting transform) [56, 57].

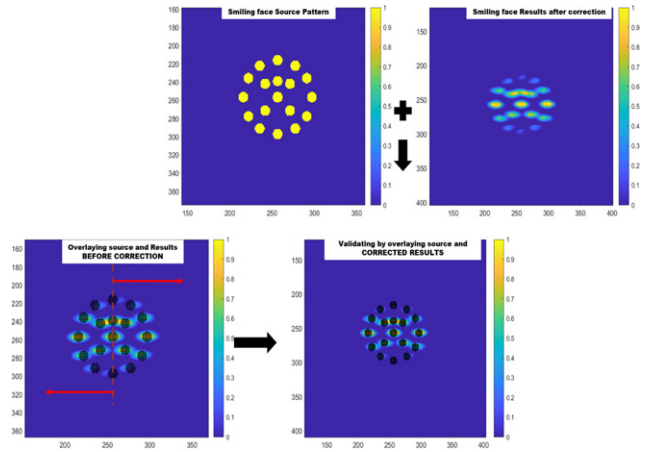

Figure 16. Perspective distortion correction validation of Twisted Slit collimator example. (Smiling face source pattern was overlaid on top of the corrected Smiling face results.)

Figure 15 shows examples of the correction algorithm applied to the final collected results. The images on the left are the raytraced convolution images for the Twisted Slit collimator, and the images on the right are the corrected images. The image corrections were confirmed using the position-based techniques where the resulting images and the source images were superimposed on each other. An example of this process is shown in Figure 16, where the Smiling face on the image titled as overlaying source and results before correction indicate the direction towards which the result is skewed/distorted.

Table II and the images in Figures 17–20 are the outcomes of the simulation experiment. From these results, the main observations are that the throughput/SNR of the Single pinhole is still better than the Twisted Slit collimator and the proposed Vortex Collimator imaging system for the same imaging conditions. Furthermore, Table III elaborates the summary of characteristics comparison between Twisted Slit collimator and Vortex Collimator. It appears that the Single Pinhole Transmittance, which is the ratio of the

Table II. Table comparing Single Pinhole with Twisted Slit Collimator and Vortex Collimator.

	Single pinhole mask			
	Pinhole source	3 Dot source	Arrow source	Smiling face source
Total flux	4.37E+05	1.11E+06	2.33E+06	7.80E+06
Ave (W/m^2):	1.75E+08	4.43E+08	9.31E+08	3.12E+09
Emitted flux (W):	7.49E+05	2.25E+06	4.49E+06	1.35E+07
Transmittance (%)	**58.41849243**	**49.32709864**	**51.82620391**	**57.87307949**
SNR	**41.2140**	**43.2323**	**44.8448**	**47.4700**

	Vortex collimator				Twisted slit collimator			
	Pinhole source	3 Dot source	Arrow source	Smiling face source	Pinhole source	3 Dot source	Arrow source	Smiling face source
Total flux	419002	1.19E+06	2.28E+06	7.04E+06	338882	619635	1.22E+06	2.93E+06
Ave (W/m^2):	1.68E+08	4.77E+08	9.10E+08	2.82E+09	1.36E+08	2.48E+08	4.89E+08	1.17E+09
Emitted flux (W):	748501	2.25E+06	4.49E+06	1.35E+07	748501	2.25E+06	4.49E+06	1.35E+07
Transmittance (%)	**55.97881633**	**53.14451124**	**50.66232317**	**52.27083797**	**45.27475581**	**27.59452238**	**27.24754565**	**21.73940474**
SNR	**41.1214**	**43.3942**	**44.7954**	**47.2489**	**40.6605**	**41.9710**	**43.4486**	**45.3439**

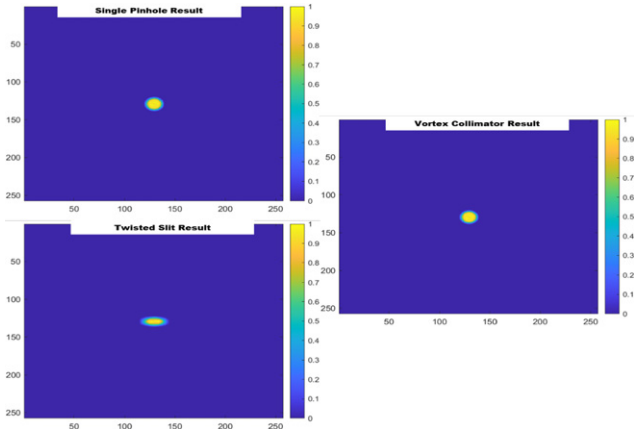

Figure 17. TracePro Simulation results for Single pinhole source with Single Pinhole Mask, Twisted Slit collimator, and Vortex Collimator.

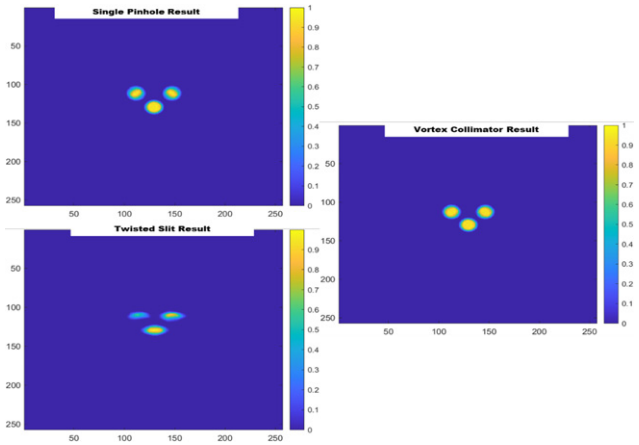

Figure 18. TracePro Simulation results for 3Dot source with Single Pinhole Mask, Twisted Slit collimator, and Vortex Collimator.

total radiant or luminous flux transmitted by a transparent object to the incident flux, averages to ∼55%, with ∼49%

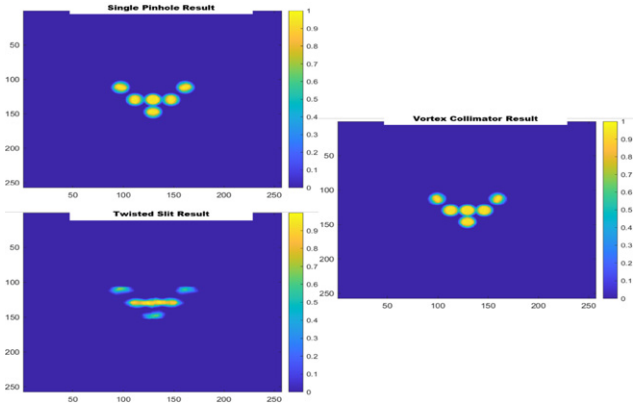

Figure 19. TracePro Simulation results for Arrow source with Single Pinhole Mask, Twisted Slit collimator, and Vortex Collimator.

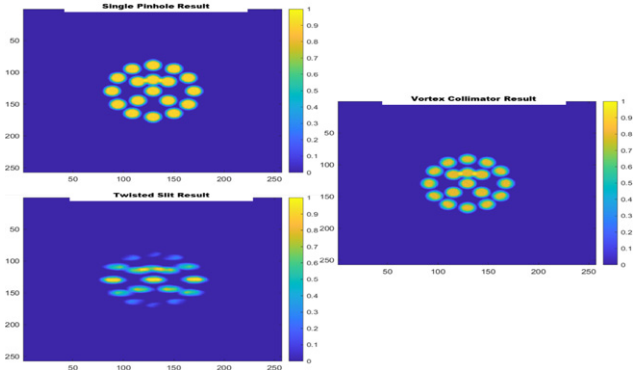

Figure 20. TracePro Simulation results for Smiling face source with Single Pinhole Mask, Twisted Slit collimator, and Vortex Collimator.

being minimum, which is still higher than the Twisted Slit collimator and newly proposed Vortex Collimator. However, Vortex Collimator transmittance averages to ∼53%, which is only about ∼2% lower than a Single pinhole system but very high compared to Twisted Slit collimator. The Twisted

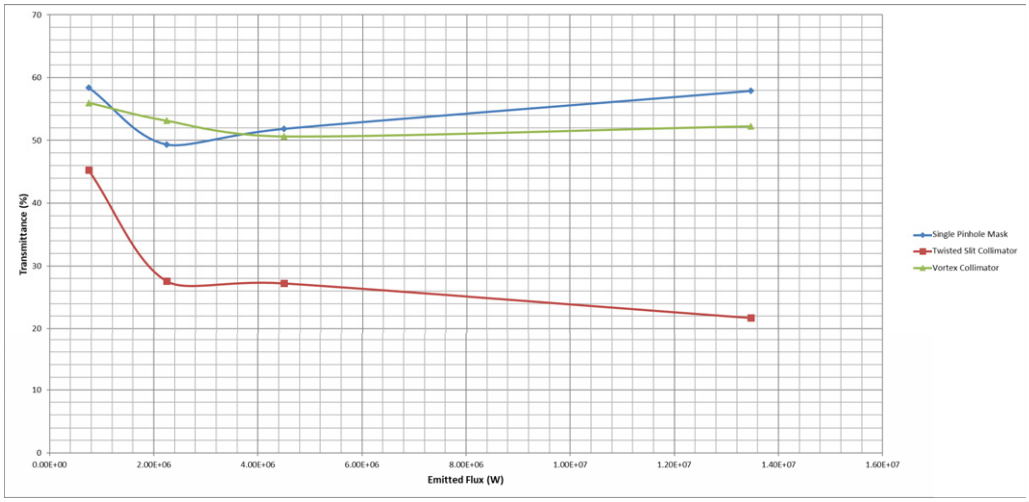

Figure 21. The comparison of transmittance between Single pinhole, Twisted Slit collimator and Vortex Collimator.

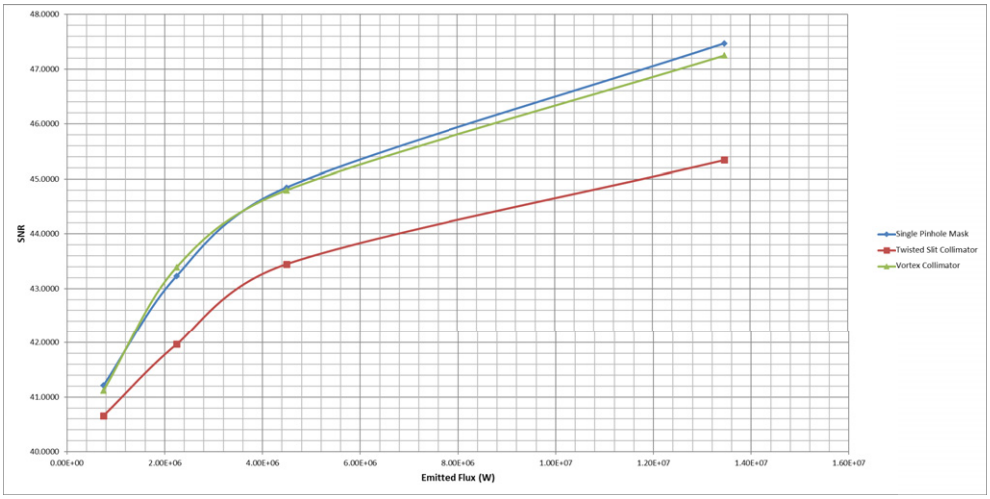

Figure 22. The comparison of SNR between Single pinhole, Twisted Slit collimator and Vortex Collimator.

Table III. Comparison of Characteristics between Twisted Slit collimator and Vortex Collimator.

Twisted Slit collimator	Vortex Collimator
Poor SNR	Better SNR
Long time to design and upload into TracePro	Easy to design and upload into TracePro
Poor transmittance	Very good transmittance
Suffers with distortion	No distortion (near zero)
Long simulation time	Fast simulation time

Slit collimator has a transmittance average of ∼30%, ∼23% lower than the Vortex Collimator.

Based on the results, comparison of characteristics shown in Tables II, III and the corresponding plots given by Figures 21, 22, the proposed Vortex Collimator system appears to have a slightly lower signal-to-noise ratio/throughput than a single pinhole system, and the transmittance is about 4% lower. However, compared to a Twisted Slit collimator, the Vortex Collimator seems to have better SNR/ throughput and significantly high transmittance, ranging between ∼10% to even ∼30% higher. Even though the Vortex Collimator is slightly lower in performance than a Single pinhole system, it can still be used as a viable replacement to a single pinhole imaging system, especially in high-energy radiation imaging conditions. Also, compared with a Twisted Slit collimator, a Vortex Collimator seems easy to design and has a shallow simulation for the same simulation conditions.

3.2 *Vortex Collimator with Different Openings*

The original Vortex Collimator was designed with a 5 mm by 5 mm opening and 1 mm exit diameter, and 50 mm thickness. Nevertheless, out of curiosity, we decided to increase and reduce the opening by two times or half times the original design. First, we reduced the opening to 2.5 mm ×2.5 mm and kept the rest of the dimensions the same as the original design and the output results are given in Figure 23. Then the

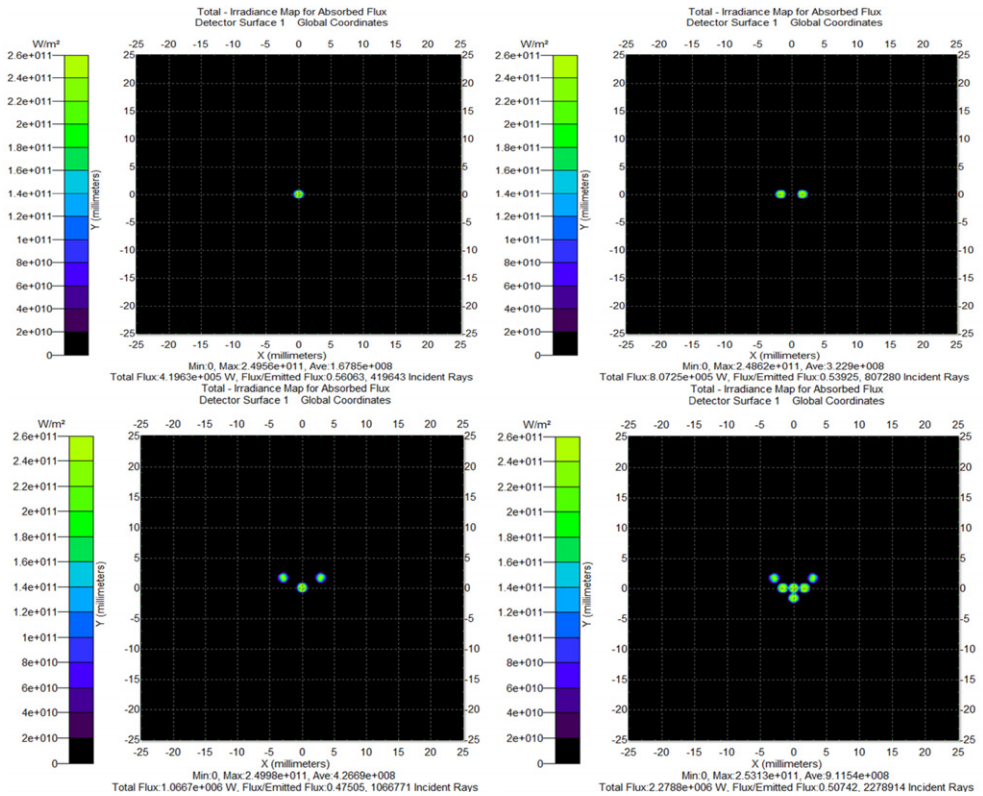

Figure 23. Vortex Collimator detector data with opening size halved (2.5 mm by 2.5 mm).

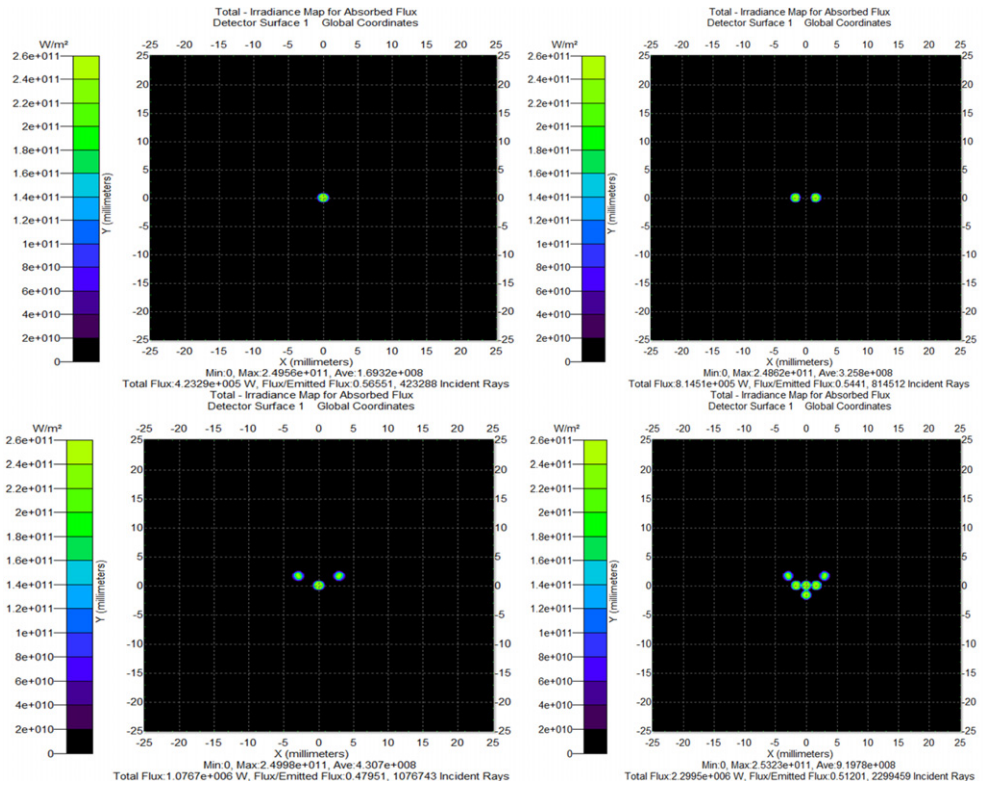

Figure 24. Vortex Collimator detector data with opening size doubled (10 mm by 10 mm).

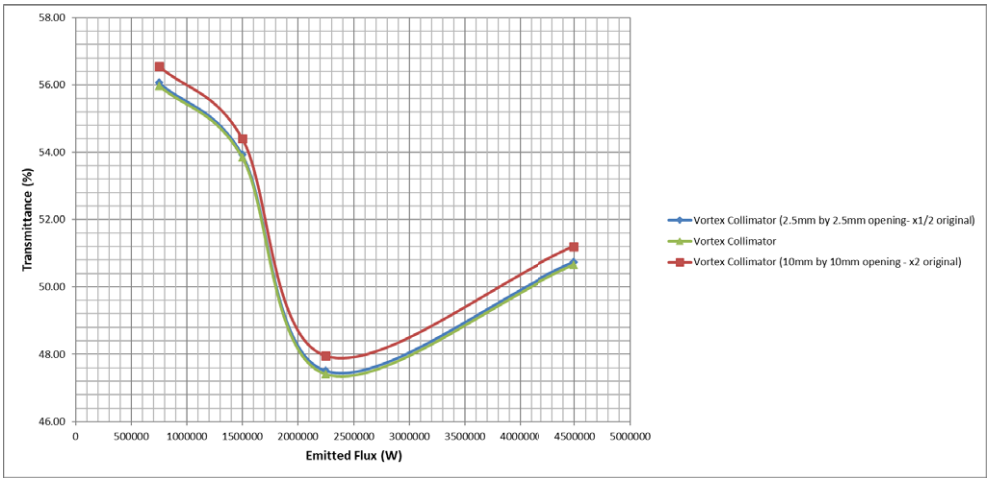

Figure 25. Vortex Collimator versus Vortex Collimator with X 1/2 opening diameter and Vortex Collimator with X 2 opening diameter transmittance comparison.

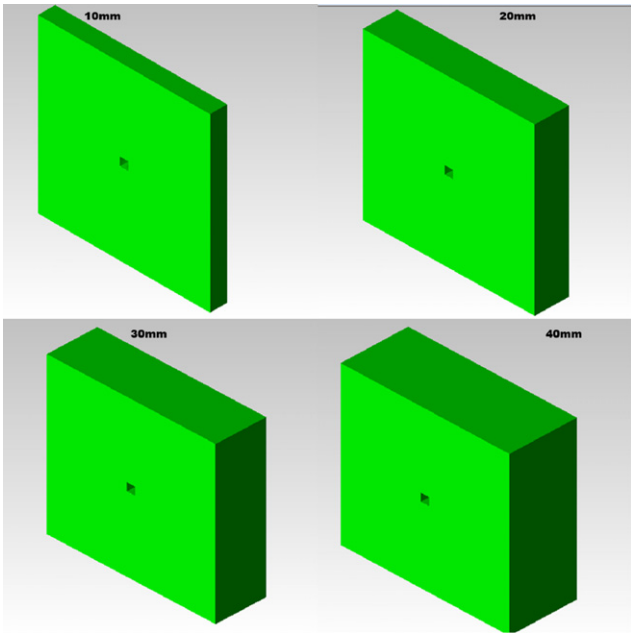

Figure 26. Example designs of Vortex Collimator with 10 mm, 20 mm, 30 mm and 40 mm thicknesses.

opening was increased to 10 mm × 10 mm, and kept the rest of the dimensions to the original design. The output for this increase is displayed in Figure 24. Moreover, these designs were compared with the original design; the table and plots are given by Table IV and Figure 25. These results show that the opening with 10 mm by 10 mm has slightly higher ∼1% transmittance than the other designs but not a noticeable improvement.

3.3 *Design Modifications and Evaluation*

As mentioned in the system design section, even though we are using a Vortex Collimator with a 50 mm × 50 mm × 50 mm cube system with a 5 mm × 5 mm opening with

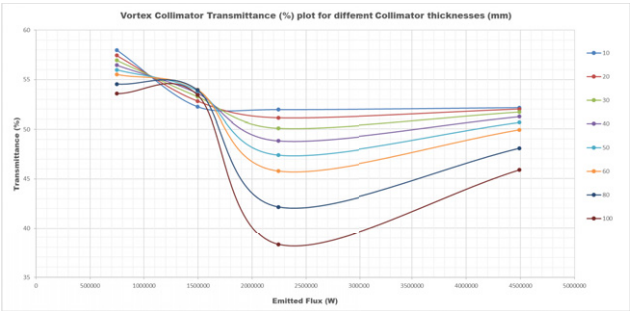

Figure 27. Vortex Collimator emitted flux (W) versus transmittance (%) plot for different Collimator thicknesses (mm).

a 1 mm exit diameter, there are other design options available. One of the possibilities is to increase or reduce the thicknesses of the systems and, secondly, increase or reduce the openings and exit diameter. To understand the effect of doing so, first, we chose a range of designs with different thicknesses varying from 10 mm to 40 mm (10 mm, 20 mm, 30 mm and 40 mm) with the same opening and same exit diameters, and later we also investigated 60 mm, 80 mm and 100 mm. Same as other designs, they were designed in Creo and uploaded into TracePro. Most importantly, the same sources and boundary conditions were used.

As mentioned in the early part of this section and the previous chapter, a 50 mm thick Vortex Collimator was used to compare with a Twisted Slit collimator currently available in the industry for NDT testing inspired the design of the Vortex Collimator. However, for further development, the thickness of the design was reduced and increased to observe the performance. Furthermore, as shown by Table V, Figures 26 and 27, on average, reducing the thickness of the Vortex Collimator increases the system's performance by ∼3% (transmittance), which is an improvement but not a significant improvement expected.

As explained in the earlier sections, the Twisted Slit design is symmetrical (isometric cube). Therefore changing

Table IV. Vortex Collimator versus Vortex Collimator with X 1/2 opening diameter and Vortex Collimator with X 2 opening diameter.

	Vortex collimator (5 mm by 5 mm opening)				Vortex collimator (2.5 mm by 2.5 mm opening – X 1/2 original)				Vortex collimator (10 mm by 10 mm opening – X 2 original)			
	Pinhole source	2 Dot source	3 Dot source	Arrow source	Pinhole source	2 Dot source	3 Dot source	Arrow source	Pinhole source	2 Dot source	3 Dot source	Arrow source
Total flux	419002	806180	1064770	2275250	419629	807251	1066720	2278840	423288	814512	1076740	2299460
Ave (W/m^2):	167601000	322472000	425908000	910102000	167852000	322900000	426688000	911537000	169315000	325805000	430697000	919784000
Emitted flux (W):	748501	1497000	2245500	4491010	748501	1497000	2245500	4491010	748501	1497000	2245500	4491910
Transmittance (%)	**55.98**	**53.85**	**47.42**	**50.66**	**56.06**	**53.92**	**47.50**	**50.74**	**56.55**	**54.41**	**47.95**	**51.20**

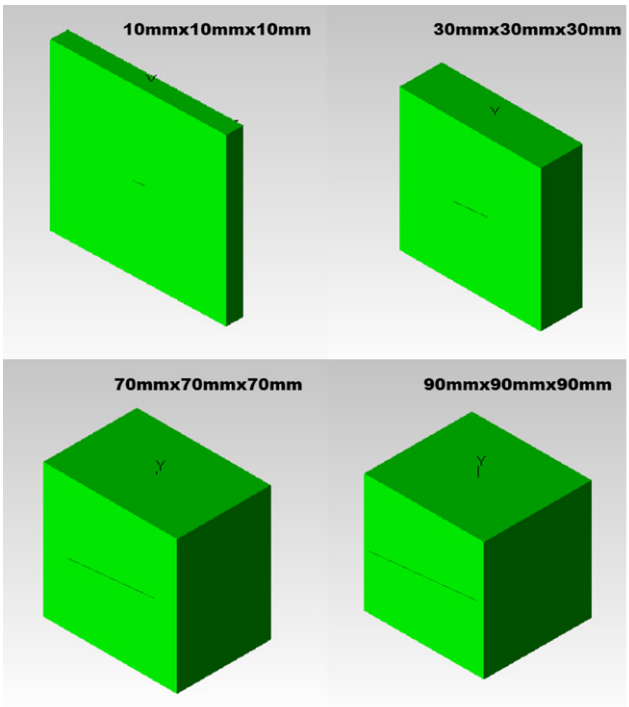

Figure 28. Twisted Slit collimators in different thicknesses.

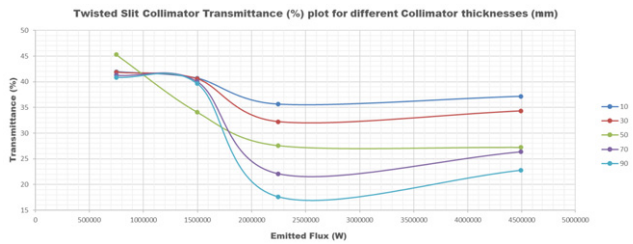

Figure 29. Twisted Slit Collimator emitted flux (W) versus transmittance (%) plot for different Collimator thicknesses (mm).

the thickness will also alter the height and width to the exact measurement as the thickness. The Fig. 26 shows a range of Twisted Slit designs with varying thicknesses.

Moreover, Table VI shows the corresponding results for different source designs, which elaborates along with Figures 28 and 29 similar to Vortex Collimator characteristics, the overall emittance of the collimator design increases by ∼6% when the thickness of the Collimator decreases.

Table V. Transmittance based on different thicknesses of Vortex Collimator.

Source	Vortex thicknesses (mm)	Transmittance (%)
Single pinhole	10	57.978
	20	57.439
	30	56.948
	40	56.459
	50	55.979
	60	55.506
	80	54.548
	100	53.587
2 Dot source	10	52.259
	20	52.82
	30	53.275
	40	53.614
	50	53.85
	60	53.977
	80	53.924
	100	53.445
3 Dot source	10	51.968
	20	51.137
	30	50.113
	40	48.854
	50	47.418
	60	45.802
	80	42.172
	100	38.268
Arrow source	10	52.168
	20	52.02
	30	51.73
	40	51.269
	50	50.662
	60	49.913
	80	48.057
	100	45.867

Table VI. Transmittance based on different thicknesses of Twisted Slit collimator.

Source	Twisted slit thicknesses (mm)	Transmittance (%)
Single pinhole	10	41.964
	30	57.847
	50	45.275
	70	41.269
	90	40.853
2 Dot source	10	40.705
	30	40.59
	50	34.106
	70	40.044
	90	39.639
3 Dot source	10	35.644
	30	32.229
	50	27.594
	70	22.082
	90	17.618
Arrow source	10	37.171
	30	34.311
	50	27.247
	70	26.352
	90	22.782

However, the results are still less satisfactory than the Vortex Collimator. Most importantly, manufacturing a cube in a size of 10 mm × 10 mm × 10 mm is not an easy task. The above statement also proves the statement made in the previous section that changing the thickness of the Twisted Slit collimator is not practicable as changing the thickness of the Vortex Collimator.

4. CONCLUSION

The Vortex Collimator is a newly introduced imaging system that is a 3-dimensional representation of an iris. The design was first designed using Creo (Pro-Engineer) CAD modelling software and then analyzed using TracePro raytracing simulation software to compare with single pinhole, which was purely for reference purposes and Twisted Slit collimator. Like for like comparison, they were designed to the exact sizes (thicknesses of 50 mm except for Single pinhole, which was 1 mm), material properties which were of Tungsten, same boundary conditions such as the wavelength of 0.0021 nm (∼600 kev), and more importantly, the same exit aperture area of 0.785 mm^2.

By proceeding further, it is clear that even though the Vortex Collimator throughput/SNR and the average transmittance values are slightly poor than the Single pinhole system (which was purely used for reference/comparison purposes and not capable of high energy radiation imaging scenarios), compared to of Twisted Slit collimator, Vortex Collimator demonstrates 4% higher SNR/Throughput and 42.5% higher transmittance than Twisted Slit collimator. Moreover, the Vortex Collimator does not suffer from any distortion as the Twisted Slit collimator does.

Additionally, in this research work, the opening was reduced to 2.5 mm ×2.5 mm and increased to 10 mm by 10 mm by keeping the rest of the dimensions the same as the original design and the output results are compared in Fig. 25 and tabulated in Table IV. These results indicate that the opening with 10 mm ×10 mm has a slightly higher transmittance of ∼1%, but it is not significant enough improvement to change the design.

For further development, the thickness of the Vortex Collimator and Twisted Slit collimator were reduced and increased to observe the performance. Furthermore, as shown by Tables V, VI, Figs. 27 and 29, on average, reducing the thickness of the Vortex Collimator increases the system's performance by ∼3% (transmittance), which is a marginal improvement and the same with Twisted Slit collimator, the overall emittance of the collimator design increases by ∼6%when the thickness of the collimator decreases. However, the results are still more unsatisfactory than the Vortex Collimator.

In conclusion, it's more likely that the Vortex Collimator is a better choice in certain situations, e.g. when high-energy radiation transmission is the most important design factor. The main advantages of using Vortex Collimator are that it is easy to fabricate, the effect of distortion artefact is shallow (near zero for axial sources) when compared to Twisted Slit collimator, sharp images/results even with smaller openings, better throughput/Signal to noise ratio, fewer design compromises (for example thickness of the design does not affect the height and width of the design, entrance opening does not affect the exit opening) and short measurement time. As the next stage of this research, we plan to fabricate the Vortex Collimator for a laboratory-based experiment and compare it with the Twisted Slit collimator in a real case scenario such as industrial based biomedical, security and NDT applications.

ACKNOWLEDGMENT

This work was generously supported by the Centre for Electronic Warfare, Information and Cyber, Cranfield University and Cooke Optics Limited.

REFERENCES

[1] G. R. Jaenisch, F. Wieder, J. Vogel, U. Ewert, C. Bellon, and M. Messerschmid, "Scatter imaging – simulation of aperture focusing by deconvolution," *Far East NDT New Technology & Application Forum (FENDT)* (IEEE, Piscataway, NJ, 2017), pp. 301–306.

[2] G. Jaenisch, S. Kolkoori, and C. Bellon, "Quantitative simulation of back scatter X-ray imaging and comparison to experiments," *19th World Conf. on Non-Destructive Testing (WCNDT)* (2016), pp. 1–11.

[3] S. Kolkoori, N. Wrobel, K. Osterloh, U. Zscherpel, and U. Ewert, "Novel X-ray backscatter technique for detection of dangerous materials: application to aviation and port security," J. Instrum. **8**, P09017 (2013).

[4] R. Hetzel, F. Mueller, J. Grahe, A. Honn, D. Schug, and V. Schulz, "Characterization and simulation of an adaptable fan-beam collimator for fast calibration of radiation detectors for PET," IEEE Trans. Radiat. Plasma Med. Sci. **4**, 538–545 (2020).

[5] A. Vella, A. Munoz, M. J. F. Healy, D. W. Lane, D. Lockley, and J. Zhou, "A fast and reliable approach to simulating the output from an X-ray tube used for developing security backscatter imaging," Proc. SPIE **10388**, 103880X (2017).

[6] L. J. Schultz, M. S. Wallace, M. C. Galassi, A. S. Hoover, M. Mocko, D. M. Palmer, S. R. Tornga, R. M. Kippen, M. V. Hynes, M. J. Toolin, and B. Harris, "Hybrid coded aperture and Compton imaging using an active mask," Nucl. Instrum. Methods Phys. Res. A Accel. Spectrom. Detect. Assoc. Equip. **608**, 267–274 (2009).

[7] H. W. Tseng, S. Vedantham, S. H. Cho, and A. Karellas, "Joint optimization of collimator and reconstruction parameters in X-ray fluorescence computed tomography using analytical point spread function and model observer," IEEE Trans. Biomed. Eng. **67**, 2443–2452 (2020).

[8] S. Kulpe, M. Dierolf, B. Gnther, J. Brantl, M. Busse, K. Achterhold, F. Pfeiffer, and D. Pfeiffer, "Physica medica spectroscopic imaging at compact inverse compton X-ray sources," Phys. Medica **79**, 137–144 (2020).

[9] H.-S. Horace, "I. Digital image processing and computer vision," Image Vis. Comput. **8** (1990).

[10] A. Faust, "Development of a coded-aperture backscatter imager using the UC San Diego HEXIS detector," AeroSense **5089**, 95–106 (2003).

[11] D. J. Brady, "Optical imaging and spectroscopy," (2009).

[12] D. R. Mcalister and D. Ph, "Gamma ray attenuation properties of common shielding materials," (2018).

[13] P. Zhu, P. Duvauchelle, G. Peix, and D. Babot, "X-ray Compton backscattering techniques for process tomography: imaging and characterization of materials," Meas. Sci. Technol. **7**, 281–286 (1996).

[14] M. Margret and M. Menaka, "Compton back scatter imaging for mild steel rebar detection and depth characterization embedded in concrete," Nucl. Instrum. (2015).

[15] S. Kolkoori, N. Wrobel, and U. Ewert, "A new X-ray backscatter technology for aviation security applications," *2015 IEEE Int'l. Symposium on Technologies for Homeland Security (HST)* (IEEE, Piscataway, NJ, 2015), pp. 1–5.

[16] N. Wrobel, S. Kolkoori, U. Zscherpel, and U. Ewert, "Innovative X-ray backscatter technique for security applications: detection of dangerous materials 2. New X-ray backscatter camera,"**1**, 1–8 (2014).

[17] Jean in 't Zand. "Coded aperture camera imaging concept," (1996).

[18] M. Galloway, A. Zoglauer, S. E. Boggs, and M. Amman, "A Combined Compton and Coded-aperture Telescope for medium-energy gamma-ray astrophysics," Astronomy & Astrophysics **614**, 1–9 (2018).

[19] V. Blahnik, B. Voelker, C. Z. Ag, V. Blahnik, and B. Voelker, "About the reduction of reflections for camera lenses How T*-coating made glass invisible," (2016).

[20] K. MacCabe, K. Krishnamurthy, A. Chawla, D. Marks, E. Samei, and D. Brady, "Pencil beam coded aperture X-ray scatter imaging," Opt. Express **20**, 16310 (2012).

[21] J. Liang, "Punching holes in light: Recent progress in single-shot coded-aperture optical imaging," Rep. Prog. Phys. **83** (2020).

[22] C. Fiorini, R. Accorsi, and G. Lucignani, "Single pinhole and coded aperture collimation systems for high-resolution gamma-ray imaging in nuclear medicine: A comparative study," IEEE Nucl. Sci. Symp. Conf. Rec. **5**, 2938–2940 (2005).

[23] R. Accorsi, F. Gasparini, and R. C. Lanza, "Coded aperture imaging," (2004).

[24] S. R. Gottesman and E. E. Fenimore, "New family of binary arrays for coded aperture imaging," Appl. Opt. **28**, 4344–4352 (1989).

[25] G. Huang, C. Geng, F. Li, J. Liu, and X. Li, "Control bandwidth promotion of adaptive fiber-optics collimator and its application in coherent beam combination," IEEE Photonics J. **10** (2018).

[26] K. Osterloh and U. Ewert, K. H. B. Patent DE 10 2005 029 674 (2008).

[27] N. Wrobel, K. Osterloh, M. Jechow, and U. Ewert, "X-ray backscattering: Variable irradiation geometry facilitates new insights," *NDT E Int.* (Bad Breisig, Germany, 2012), pp. 16–20.

[28] S. Kolkoori, N. Wrobel, U. Zscherpel, and U. Ewert, "A new X-ray backscatter imaging technique for non-destructive testing of aerospace materials," NDT E Int. **70**, 41–52 (2015).

[29] S. Kolkoori, N. Wrobel, U. Zscherpel, and U. Ewert, "A new X-ray backscatter imaging technique for non-destructive testing of aerospace materials," NDT E Int. **70**, 41–52 (2015).

[30] R. C. Gonzalez, R. E. Woods, and S. L. Eddins, "Digital image processing using Matlab," Education **624**, 609 (2004).

[31] R. C. Gonzalez and R. E. Woods, *Digital Image Processing* (Pearson Education, 2011), Vol. 21.

[32] A. Ihsani and T. Farncombe, "An adaptation of the distance driven projection method for single pinhole collimators in SPECT imaging," IEEE Trans. Nucl. Sci. **63**, 140–150 (2016).

[33] I. Odinaka, J. A. Greenberg, Y. Kaganovsky, A. Holmgren, M. Hassan, D. G. Politte, J. A. O'Sullivan, L. Carin, and D. J. Brady, "Coded aperture X-ray diffraction imaging with transmission computed tomography side-information," Proc. SPIE **9783**, 978323 (2016).

[34] Z. Chen, C. Zhang, T. Mu, T. Yan, D. Bao, Z. Chen, and Y. He, "Coded aperture snapshot linear-Stokes imaging spectropolarimeter," Opt. Commun. **450**, 72–77 (2019).

[35] D. J. Ching, S. Aslan, V. Nikitin, M. J. Wojcik, and D. Gursoy, Evaluation of modified uniformly redundant arrays as structured illuminations for ptychography. Preprint arXiv:2004.01766 .

[36] J. Lee, H. Hiraka, and S. Cho, "Development of triple-axis spectrometer device in HANARO: Numerical simulation results on mirror-type collimators," IEEE Trans. Magn. **55**, 2019–2022 (2019).

[37] Y. Li, S. Matej, J. S. Karp, and S. D. Metzler, "Model-based normalization of a fractional-crystal collimator prototype for small-animal PET imaging," IEEE Nucl. Sci. Symp. Conf. Rec. **1**, 262–267 (2013).

[38] McGraw-Hill Dictionary of Scientific & Technical Terms. "Transmission factor | article about transmission factor by the free dictionary," (The McGraw-Hill Companies, Inc. 2003).

[39] R. Accorsi and R. C. Lanza, "High-sensitivity dynamic coded aperture imaging," *2003 IEEE Nuclear Science Symposium. Conf. Record (IEEE Cat. No. 03CH37515)* (IEEE, Piscataway, NJ, 2003), Vol. 3, pp. 1833–1837.

[40] D. M. Starfiel, "Towards clinically useful coded apertures for planar nuclear medicine imaging," Phys. Med. Biol. **36**, 125–133 (2020).

[41] L. Pedrotti, "Basic geometrical optics," *Fundamentals of Photonics* (SPIE, Bellingham, WA, 2008).

[42] Q. Tang, G. L. Zeng, and Q. Huang, "An analytical algorithm for skew-slit collimator SPECT with uniform attenuation correction," Phys. Med. Biol. **51**, 6199–6211 (2006).

[43] J. M. Mountz, "Gamuts in nuclear medicine, 2nd ed.," Clin. Nucl. Med. **15**, 58–59 (1990).

[44] A. G. Hassan, H. Elkady, A. S. Faried, M. A. Hassan, and M. E. Allam, "Evaluation of electric arc furnace slag high strength shielding concrete on exposure to gamma 662 KeV," Case Stud. Constr. Mater. **13**, e00416 (2020).

[45] J. Jain, J. Moreno, S. Davis, B. Bora, C. Pavez, G. Avaria, and L. Soto, "Experimental measurements of high-energy photons in X-rays pulses emitted from a hundred joules plasma focus device and its interpretations," Results Phys. **16**, 102915 (2020).

[46] I. Ozsahin, L. Chen, A. Knik, M. A. King, F. J. Beekman, and G. S. Mok, "The clinical utilities of multi-pinhole single photon emission computed tomography," Quantum Imaging Med. Surg. **10**, 2006–2029 (2020).

[47] S. Russo, L. Masi, P. Francescon, P. Dicarolo, E. De Martin, M. C. Frassanito, I. Redaelli, S. Vigorito, M. Stasi, and P. Mancuso, "Physica Medica Multi-site evaluation of the Razor stereotactic diode for CyberKnife small field relative dosimetry," Phys. Medica **65**, 40–45 (2019).

[48] S. Russo, L. Masi, P. Francescon, M. C. Frassanito, M. L. Fumagalli, M. Marinelli, M. D. Falco, A. S. Martinotti, M. Pimpinella, G. Reggiori, and G. V. Rinati, "Physica Medica Multicenter evaluation of a synthetic single-crystal diamond detector for CyberKnife small field size output factors," Phys. Medica **32**, 575–581 (2016).

[49] R. Fischer, S. Perkins, A. Walker, and E. Wolfart, "Geometric operations – affine transformation", (2004).

[50] A. Coste, "CS 6640: image processing project 3 affine transformation, landmarks registration, non linear warping," (2012).

[51] D. House and J. C. Keyser, "Foundations of physically based modeling and animation," Found. Phys. Based Model. Animat. (2016).

[52] C. Andrei, "3D affine coordinate transformations," Geometria (2006).

[53] Z. T. Harmany, R. F. Marcia, and R. M. Willett, "Compressive coded aperture keyed exposure imaging with optical flow reconstruction". Preprint arXiv:1306.6281 (2013).
[54] R. Kawakami, Y. Matsushita, J. Wright, M. Ben-Ezra, Y. W. Tai, and K. Ikeuchi, "High-resolution hyperspectral imaging via matrix factorization," *Proc. IEEE Comput. Soc. Conf. Comput. Vis. Pattern Recognit.* (IEEE, Piscataway, NJ, 2011), pp. 2329–2336.
[55] R. Horaud, B. Conio, O. Leboulleux, and B. Lacolle, Comput. graph. image process. **47**, 33–44 (1989).
[56] V. Tyagi, "Understanding digital image processing," *Underst. Digit. Image Process.* (CRC Press, Boca Raton, FL, 2018).
[57] M. E. Antohe, D. A. Forna, C. G. Dascalu, and N. C. Forna, "Implications of digital image processing in the paraclinical assessment of the partially edentated patient," Rev. Chim. (Bucharest) **69** (2018).